AGU PUBLICATIONS

JGR

Journal of Geophysical Research: Earth Surface

RESEARCH ARTICLE
10.1002/2015JF003618

Key Points:
- Strike-slip landscapes are in permanent disequilibrium from river lengthening and capture
- Hillslope ridges upstream of slow-slipping strike-slip faults migrate laterally
- A recognizable suite of geomorphic signatures can indicate horizontal fault slip rate

Supporting Information:
- Table S1
- Movie S1
- Movie S2
- Movie S3
- Text S1

Correspondence to:
A. R. Duvall,
aduvall@uw.edu

Citation:
Duvall, A. R., and G. E. Tucker (2015), Dynamic Ridges and Valleys in a Strike-Slip Environment, *J. Geophys. Res. Earth Surf.*, *120*, 2016–2026, doi:10.1002/2015JF003618.

Received 29 MAY 2015
Accepted 27 AUG 2015
Accepted article online 2 SEP 2015
Published online 3 OCT 2015

Dynamic Ridges and Valleys in a Strike-Slip Environment

Alison R. Duvall[1] and Gregory E. Tucker[2]

[1]Department of Earth and Space Sciences, University of Washington, Seattle, Washington, USA, [2]CIRES and Department of Geological Sciences, University of Colorado, Boulder, Colorado, USA

Abstract Strike-slip faults have long been known for characteristic near-fault landforms such as offset rivers and strike-parallel valleys. In this study, we use a landscape evolution model to investigate the longer-term, catchment-wide landscape response to horizontal fault motion. Our results show that strike-slip faulting induces a persistent state of disequilibrium in the modeled landscapes brought about by river lengthening along the fault alternating with abrupt shortening due to stream capture. The models also predict that, in some cases, ridges oriented perpendicular to the fault migrate laterally in conjunction with fault motion. We find that ridge migration happens when slip rate is slow enough and/or soil creep and river incision are efficient enough that the landscape can respond to the disequilibrium brought about by strike-slip motion. Regional rock uplift relative to baselevel also plays a role, as topographic relief is required for ridge migration. In models with faster horizontal slip rates, stronger rocks, or less efficient hillslope transport, ridge mobility is limited or arrested despite the continuance of river lengthening and capture. In these cases, prominent steep, fault-facing facets form along well-developed fault valleys. Comparison of landscapes adjacent to fast-slipping (>30 mm/yr) and slower-slipping (≤1 mm/yr or less) strike-slip faults in California, USA, reveals features that are consistent with model predictions. Our results highlight a potential suite of geomorphic signatures that can be used as indicators of horizontal crustal motion and geomorphic processes in strike-slip settings even after river capture has diminished or erased apparent offset along the fault.

1. Introduction

Strike-slip faults, which are among the straightest and longest geologic features on Earth, are often identified by their geomorphic expression, including hallmarks such as offset rivers, shutter ridges, sag ponds, and linear, strike-parallel valleys [e.g., *Wallace*, 1949; *Hill and Dibblee*, 1953]. Detailed mapping and dating of such features offer a means for determining fault location and, in the best cases, slip rates. Fault slip rate estimates form the cornerstone of most paleoseismological and neotectonic studies, as they are instrumental in assessing earthquake hazards, understanding the mechanics of fault zones, and determining changes in fault behavior over time. Slip rates along major faults are commonly found by measuring the magnitude of displacement and the timing of offset landforms such as rivers or river terraces [e.g., *Weldon and Sieh*, 1985; *Berryman*, 1990; *Mann et al.*, 1998; *Hubert-Ferrari et al.*, 2002; *Van der Woerd et al.*, 2002; *Mériaux et al.*, 2004; *Cowgill*, 2007], especially along strike-slip faults where piercing points are sharp and well defined. Although simple in principle, complications with this approach arise from the challenges and uncertainty in dating of landforms as well as ambiguities in terrace-riser reconstructions [*Cowgill*, 2007; *Gold et al.*, 2009]. Additional difficulties occur in regions where river channels are ephemeral or catchments are young and evolving. In these settings, rivers might not predate fault motion and thus record only a small portion of the fault offset [*Lacassin et al.*, 1998].

Despite the obvious imprint of strike-slip faulting on Earth's surface and the challenges to interpreting this record, few studies have gone beyond the first-order, near-fault tectonic landforms to understand the longer-term geomorphic process response to prolonged lateral motion. Cumulative effects of faulting over many earthquake cycles are known to affect fluvial systems and lead to difficulties in interpreting the geomorphic record [e.g., *Lacassin et al.*, 1998; *Hubert-Ferrari et al.*, 2002; *Zielke et al.*, 2010; *Walker and Allen*, 2012]. Flume experiments designed to assess river channel reaction to horizontal fault displacement show downstream degradation and upstream aggradation in addition to lateral channel shifts with progressive fault motion [*Ouchi*, 2004]. If, how, and when such near-fault perturbations to the fluvial system affect the upstream catchment has yet to be explored in detail. In addition, although streams that cross an active

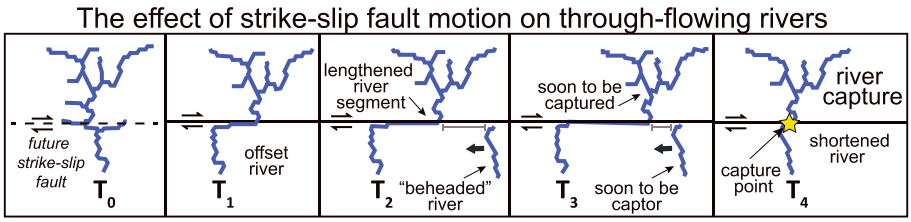

Figure 1. Schematic illustration of stages of gradual river lengthening due to fault offset (T1–T3) and abrupt shortening due to river capture (T4) along a strike-slip fault.

strike-slip fault can be excellent offset markers, continued fault slip often leads to stream capture, which reduces or erases the apparent offset, leading to underestimates of fault slip rates [*Lacassin et al*., 1998]. Sustained horizontal motion should, in theory, drive persistent landscape disequilibrium for as long as fault motion continues. Cycles of gradual stream lengthening along the fault followed by abrupt shortening and increased incision due to stream capture are expected to occur in catchments that drain to or across active strike-slip faults [*Wallace*, 1968; *Gaudemer et al*., 1989; *Huang*, 1993; *Replumaz et al*., 2001; *Hubert-Ferrari et al*., 2002; *Ouchi*, 2005] (Figure 1). Recent field [*Dorsey and Roering*, 2006; *Walker and Allen*, 2012] and numerical [*Goren et al*., 2014] studies offer some support to these first-order predictions. Still, the long-term impacts of strike-slip faulting, both near-fault and upstream, remain poorly understood and underexplored.

Over the long term, the collective effects of river lengthening and shortening should propagate into river reaches far upstream of fault zones, imparting widespread and lasting impact on surrounding landscapes. Information related to fault timing and slip rate may thus be recorded in headwater basins where evidence would be preserved for longer periods of time. Here we investigate the development and morphology of strike-slip landscapes under varying slip rates, bedrock erodibility, and hillslope transport efficiency in order to evaluate the long-term landscape response to horizontal fault motion and our ability to extract fault information from the landscape. We address this problem numerically using a landscape evolution model. We then compare our results to well-known strike-slip faults in California, USA, that experience order of magnitude differences in slip rate.

2. Model Description

We focus on eroding landscapes in which a series of parallel drainage basins are crossed by a strike-slip fault, such that the drainages are initially aligned roughly perpendicular to the fault strike (Figure 1). The model includes a simple representation of erosion by two processes: channel incision and hillslope soil creep. The rate of stream incision is assumed to be proportional to unit stream power [*Seidl and Dietrich*, 1992; *Howard*, 1994; *Whipple and Tucker*, 1999], with contributing drainage area serving as a proxy for water discharge. Gravitational transport by soil creep is treated using either a linear [*Culling*, 1960] or nonlinear [*Andrews and Bucknam*, 1987; *Roering et al*., 1999] creep-transport law.

In generic form, the governing equation for the time rate of change of land-surface elevation, h, can be written as

$$\frac{\partial h}{\partial t} = B - V\frac{\partial \mathrm{h}}{\partial \mathrm{x}} - E_f - E_h \tag{1}$$

where t is time, B is the rate of baselevel lowering, V is lateral tectonic advection rate, E_f is the incision rate due to channelized flow, and E_h is the erosion (or deposition) rate due to soil creep. For the purposes of the equations in this paper, lateral advection is in the x direction. We assume that the channelized flow erosion rate is proportional to stream power per unit bed area, which is approximated as a function of channel slope, S, and drainage area, A:

$$E_f = KA^{1/2}S \tag{2}$$

where K is a rate coefficient with dimensions of 1/time and drainage area appears as a proxy for discharge per unit channel width [*Whipple and Tucker*, 1999]. In the numerical implementation, drainage area is calculated using a steepest-descent algorithm [*Tucker et al*., 2001a].

Soil creep is represented using the mass-conservation law:

$$E_h = \nabla q_s \tag{3}$$

where the soil flux per unit width, q_s, is represented either with the linear transport law:

$$q_s = -D\nabla h \tag{4a}$$

or the nonlinear law:

$$q_s = \frac{-D\nabla h}{\left(1 - \left[\frac{\nabla h}{S_c}\right]^2\right)} \tag{4b}$$

where D (with dimensions of length^2/time) is the rate coefficient for gravitational (hillslope) mass transport and S_c is an effective threshold slope gradient [*Andrews and Bucknam*, 1987; *Roering et al*., 1999].

2.1. Nondimensionalization

In order to identify which individual variables are most relevant to the evolving strike-slip-influenced landscape as well as to assess how the variables relate to one another in these systems, we nondimensionalize the governing equation. First, we consider a one-dimensional form of the governing equation, using the linear form of creep law:

$$\frac{\partial h}{\partial t} = B - V\frac{\partial \mathrm{h}}{\partial \mathrm{x}} = KA^{\frac{1}{2}}\frac{\partial \mathrm{h}}{\partial \mathrm{x}} + D\frac{\partial^2 \mathrm{h}}{\partial \mathrm{x}^2} \tag{5}$$

The quantities x, h, and, and $A^{1/2}$ are normalized with a characteristic length scale, the hillslope length, which gives the following dimensionless quantities:

$$h' = \frac{h}{L}, x' = \frac{x}{L}, A' = A/L^2 \tag{6}$$

Time is normalized with a characteristic time scale, T, so that $t' = t/T$. Introducing these gives a dimensionless form of the 1-D equation above:

$$\frac{\partial h'}{\partial t'} = \frac{BT}{L} - \frac{VT}{L}\frac{\partial \mathrm{h}'}{\partial \mathrm{x}'} + KTA'^{\frac{1}{2}}\frac{\partial \mathrm{h}'}{\partial \mathrm{x}'} + \frac{DT}{L^2}\frac{\partial^2 \mathrm{h}'}{\partial \mathrm{x}'^2} \tag{7}$$

For the length scale L we use the characteristic hillslope length, defined as

$$L = \sqrt{\frac{D}{K}} \tag{8}$$

We further define the characteristic time scale as the time required for strike-slip motion to create offset of one hillslope length:

$$T = \frac{\sqrt{D/K}}{V} \tag{9}$$

Using these definitions, the dimensionless form of the 1-D governing equation becomes

$$\begin{aligned}\frac{\partial h'}{\partial t'} &= \frac{B}{V} - \frac{\partial \mathrm{h}'}{\partial \mathrm{x}'} + \frac{\sqrt{DK}}{V}\left(A'^{\frac{1}{2}}\frac{\partial \mathrm{h}'}{\partial \mathrm{x}'} + \frac{\partial^2 \mathrm{h}'}{\partial \mathrm{x}'^2}\right) \\ &= N_{ua} - \frac{\partial \mathrm{h}'}{\partial \mathrm{x}'} + \frac{1}{\sqrt{N_{ae}}}\left(A'^{\frac{1}{2}}\frac{\partial \mathrm{h}'}{\partial \mathrm{x}'} + \frac{\partial^2 \mathrm{h}'}{\partial \mathrm{x}'^2}\right)\end{aligned} \tag{10}$$

Two dimensionless numbers determine the behavior of this equation. The advection-uplift number, N_{au}, describes the rate of horizontal fault slip relative to regional baselevel lowering rate

$$N_{\mathrm{au}} = \frac{V}{B} \tag{11}$$

and the advection-erosion number, N_{ae}, describes the speed of strike-slip motion relative to the rate with which geomorphic processes are able to reshape the terrain as it deforms:

$$N_{ae} = \frac{V^2}{KD} \tag{12}$$

The use of the nonlinear form of the creep law introduces a third dimensionless parameter, which is the threshold slope, S_c. The expected value of the threshold slope is reasonably well constrained to values on the order of 0.6 to 0.9 (~30° to ~42°).

2.2. Numerical Implementation

These equations are implemented numerically using the Channel-Hillslope Integrated Landscape Development model (CHILD), an open-source C++ code described in detail in *Tucker et al.* [2001a, 2001b]. The equations are solved using a finite difference method on an irregular (Delaunay/Voronoi) grid. The model configuration in this study consisted of an elongated grid (4000 m × 200 m with 5 m resolution), in which one of the long sides was treated as an open, fixed-elevation boundary, while the other sides were treated as closed boundaries (representing fixed drainage divides). We position the fault away from the lower grid boundary (75 m) in order to observe behavior of the river both upstream and downstream of the fault. Progressive strike-slip dislocation was modeled by laterally shifting grid points on one side of a specified y coordinate at a prescribed rate and updating the grid triangulation when needed [*Tucker et al.*, 2001b]. In addition to strike-slip motion, a uniform baselevel lowering rate was applied across the entire model domain.

In order to explore the parameter space, solutions to these equations were realized for 79 separate strike-slip model runs (Table S1 in the supporting information). Each run was initialized by first applying steady, uniform uplift relative to baselevel at 1 mm/yr until a condition of topographic steady state was reached; then, strike-slip dislocation was activated. After the onset of strike-slip fault motion, uplift continued at the same rate in order to maintain relief. No relative vertical motion occurred at any time across the fault. We also ran a subset of models with a larger grid size, higher grid resolution, and a lower uplift rate of 0.5 mm/yr to assess model sensitivity.

Models were run until 500 m of total right-lateral fault offset occurred, with each output interval representing 10 m of displacement. In each run, the erosivity and climate (represented by K and D) and fault slip rate were held constant. Modeled slip rates ranged from 0.5 to 20 mm/yr with K and D values ranging from 117 to 468×10^{-6}/yr and 0.004 to 0.016 m^2/yr, respectively. Models with nonlinear soil creep included a critical slope gradient (S_c) of 0.7. A full description of all model parameters can be found in Table S1.

2.2.1. Note on Space and Time Discretization

Kooi and Beaumont [1994], among others, have noted that drainage divides represent mathematical singularities at which drainage area is zero and fluvial erosion is ineffective. As a result, when grid cells in a landscape evolution model are larger than the length of a hillslope, certain numerical solution methods have the potential to introduce a grid-size influence on rates of divide migration. In the case of the present study, grid cells are significantly smaller than the length of a hillslope. This means that the motion of divides in the numerical model is controlled, as it should be, by hillslope processes, and does not suffer from grid-size dependence. To confirm this, we conducted runs with varying grid size and resolution (runs 71–76; Table S1) and we find as expected that there is no systematic bias in the results (see supporting information).

Time stepping in the CHILD model is handled in the following way. The three processes of soil creep, fluvial erosion, and tectonic/baselevel motion are calculated sequentially for each of a series of global time steps. Each global time step includes a period of active water flow and a period of no flow; creep and tectonic processes are calculated for the entire duration of the global time step, while fluvial processes are calculated only for the duration of the flow period (representing the fraction of the total time that runoff is sufficiently large to drive water erosion; see *Tucker and Bras* [2000] and *Tucker* [2004]). During the calculation of creep transport, the global time step is subdivided as needed to ensure numerical stability; the length of these substeps is calculated either from the standard Courant stability criterion for a finite-volume approximation to linear diffusion [see, e.g., *Press et al.*, 1992] or for an approximated stability criterion that accounts for accelerated creep on steep slopes in the nonlinear creep law. Likewise, the numerical approximation to the fluvial erosion law uses substeps that ensure numerical stability; each substep is shorter than the length of time required to reverse the gradient between an upstream-downstream node pair.

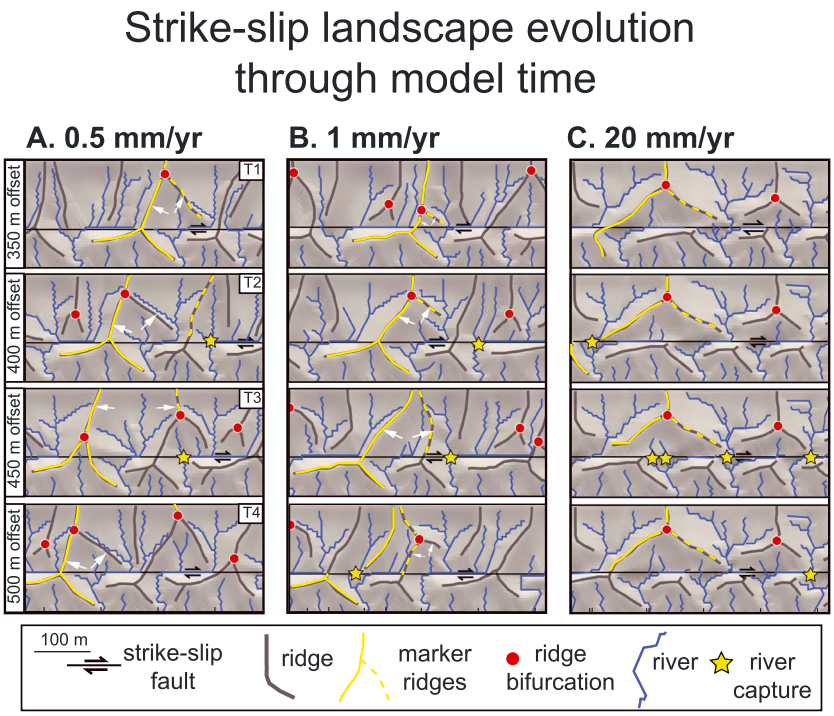

Figure 2. Model output through time from 350 to 500 m of total offset for (a) 0.5 mm/yr, (b) 1 mm/yr (B), and (c) 20 mm/yr right-lateral fault slip rate cases (see Table S1 for model parameters). Small white arrows depict the direction of catchment expansion. Note the variability in ridge spacing and the position of ridge bifurcations (red circle) at lower slip rate as compared to the more stable, faster-slip landscape. Yellow marker ridge depicts the dynamic versus static behavior of fault-perpendicular hillcrests in the slower and faster-slip cases. See Movies S1–S3 to watch full progression of landscape in response to strike-slip faulting.

3. Model Results

In all of our model experiments, landscapes evolved through time in a continuous cycle similar to that depicted in Figure 1, developing obvious fault valleys even without incorporating fault damage or strain localization to weaken materials [*Koons*, 1994; *Roy et al*., 2015]. Rivers that crossed the fault were progressively offset by strike-slip motion until a neighboring river was in position to capture the upstream headwaters. Captures occurred abruptly, resulting in shortened and straightened channels that once again lengthened as fault motion continued (Figure 2 and Movies S1–S3). Although all of the model outputs show the same general form of fault valleys and offset rivers, distinct differences in landscape morphology developed among scenarios with variable fault slip rate and erosive efficiency.

The most surprising and counterintuitive results occurred when horizontal slip rate was relatively slow and/or erosion processes were relatively efficient. Under these conditions, ridgelines upstream of the fault appear to migrate in step with the opposite fault block (Figures 2a and 2b). This phenomenon reflects the growth of new catchments that initiate along the fault-lengthened channel. As the main trunk stream grows laterally, headward erosion initiates from the new local baselevel, spurring development of nascent catchments that grow longer and wider as they expand toward the main divide through time (Figure 2 and Movies S1 and S2). Neighboring subbasins lose drainage area, shrink, and in some cases disappear at the expense of adjacent growing catchments. Fault-perpendicular ridges migrate and bifurcate as part of this process, leading to variability in valley widths, ridge positions, and catchment area within the watershed (Figures 2 and 3a).

Although ridges migrate in multiple directions, the major ridges, those that originally stretched from the main drainage divide to across the fault, move in the direction of stream lengthening along the fault (see yellow ridge marker in Figures 2a and2b and Movies S1 and S2). This happens as a consequence of new catchment growth nucleating in the direction of lengthening, at the edge of the fault-parallel river. As a result, when hillcrest migration occurs at a rate similar to that of fault slip (Figures 2a and 2b) ridges on opposite sides of the fault maintain connection even as the crustal blocks are offset laterally. Ridges

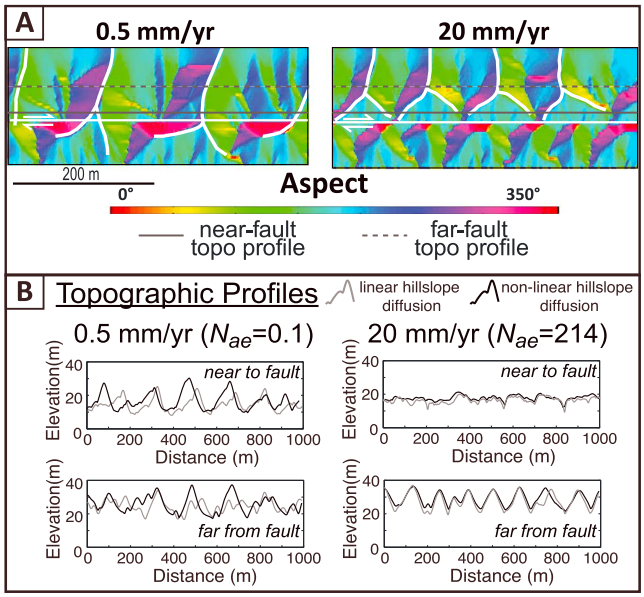

Figure 3. (a) Aspect maps of the 0.5 mm/yr and 20 mm/yr strike-slip modeled landscapes. The fast-slip case (right) shows obvious fault-facing facets and juxtaposition of ridges across the fault. The slow-slip case (left) shows ridges that extend across the fault and a higher number of catchment subbasins upstream of the fault. (b) Strike-parallel topographic profiles near to and farther from fault for the slow (left) and fast (right) slip-rate cases. Solid and dashed lines depict locations of topographic profiles in Figure 3b. Gray and black profiles represent linear and nonlinear hillslope transport models.

then only appear offset across the fault during river capture events (Figure 2, yellow stars). After a capture, they realign, appearing continuous once again as they migrate together (Figure 2b and Movie S2). In some instances in slower-slip models, river capture was impeded, allowing a single ridge to maintain continuous connection across the fault for far distances (Figure 2a, yellow marker ridge). Rivers can evade capture when a subbasin shrinks and disappears before the approaching channel on the down-stream fault block has a chance to breach the divide (Movie S1). Catchment reorganization is most vigorous at lower slip rates. Thus, the number of river captures decreases with fault slip rate (Figure 2, yellow stars).

Output from model runs with higher fault slip rates (>1 mm/yr) and/or less efficient erosion shows a less dynamic watershed response to strike-slip motion. These cases exhibit a marked reduction or absence in upstream catchment reorganization. Trunk channels still lengthen with fault motion but new tributary development from this new local base level is either absent or limited to the near-fault area. As a consequence, positions of ridgelines and junctions are relatively constant through time in the headwaters (Figure 2, right column and Movie S3) and ridges are offset sharply across the fault. In contrast to slow-slip cases, ridges in fast-slip models only appear aligned across the fault when they are juxtaposed briefly as they move past one another in opposite directions.

A plot of the standard deviation (1σ) of ridge spacing through model time for the 0.5 mm/yr through 20 mm/yr strike-slip cases reflects the observed differences in ridge mobility among models (Figure 4). Strike-slip faults that slip at slower rates (0.5–1 mm/yr) show a high degree of variability in mean ridge spacing as the model progresses, with the standard deviation ranging from 9 to 69 m throughout the model run (Figure 4). Conversely, the standard deviation of mean ridge spacing along faults that slip at faster rates remains relatively steady, with the fastest slip-rate case (20 mm/yr) holding roughly constant at ~15 m throughout the duration of the run (Figure 4).

Slope patterns also vary among different modeled scenarios. Early on in all of the experiments, steep, faceted slopes form adjacent to the fault on the upstream block as a result of breaking a discontinuity across the flank of a preexisting mountain range as well as from the formation of fault-parallel river reaches flowing along the new mountain front. In slow-slip and/or highly erosive models this pattern changes as soon as the upstream catchments begin growing and shrinking in response to fault motion, ultimately erasing any fault-facing facets that formed along the upstream block. In fast-slip and/or inefficient erosion models, which do not exhibit subbasin adjustments and ridge migration, the steepened slopes stay concentrated near the fault, giving rise to enduring fault-facing facets even in the absence of dip-slip motion (Figure 3a).

These observed differences in landscape morphology can be compared among models in order to explore the predicted relationships among slip rate, bedrock erodibility, and hillslope transport efficiency (N_{ae}). Although changes in ridge spacing through time could serve as a proxy for the degree of ridge mobility (Figure 4), comparisons of hillslope spacing through time are difficult to make in real-world settings where

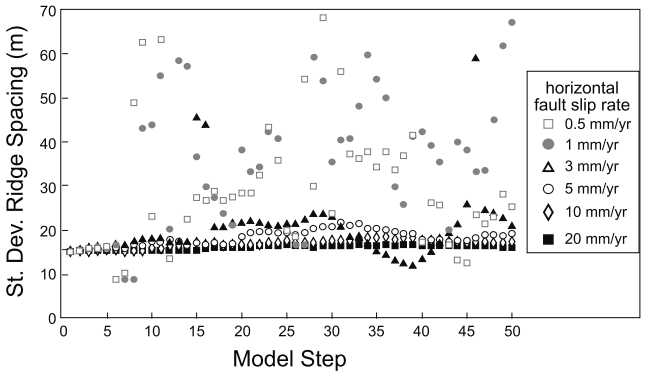

Figure 4. Plot of the standard deviation (1σ) of ridge spacing along topographic profile C (see Figure 3) through the duration of the model runs (steps 1–50) for models with slip rate varying from 0.5 to 20 mm/yr (models 17–22—Table S1). Variability in ridge spacing arises as part of the catchment reorganization and ridge migration driven by strike-slip faulting (see text for more details); thus, standard deviation of ridge spacing through time provides a useful metric for assessing this behavior in modeled landscapes. Note the high degree of variability in ridge spacing for the slow-slip cases (high standard deviation) versus the relatively steady spacing at the higher slip rates (lower and constant standard deviation) that reflects differences in ridge mobility.

paleoridge spacing cannot be measured easily. As a more practical alternative, we capture a snapshot of the response to strike-slip motion with a metric termed the "profile relief ratio" (PRR). PRR is calculated by dividing the maximum local relief found along a topographic profile close to the fault (within 12 m in the upstream direction) by the maximum local relief found along a topographic swath profile farther upstream from the fault (between 30 and 60 m). Profile relief ratios should reflect the dichotomy of landscape response to strike-slip faulting because catchments with steep fault-facing slopes (static upstream response) will have lower relief ratios than those without facets, which instead have ridges that extend to and across the fault (dynamic upstream response). Thus, PRR serves as an indirect measure of the degree of new catchment growth and ridge mobility. A lower PRR (<1) reflects little to no ridge mobility, whereas a higher PRR (~1) reflects a high degree of ridge mobility. The 0.5 mm/yr and 20 mm/yr slip-rate experiments show these expected variations in PRR (Figure 3). The near and far topographic profiles for the 0.5 mm/yr case share similar high relief, yielding a calculated PRR of 1 (Figure 3b, left and Figure 5, inset). In comparison, the 20 mm/yr case shows muted relief in the near fault topographic profile (Figure 3b, right) but higher relief far from the fault, which results in a lower PRR of 0.4 (Figure 5, inset).

A plot of PRR versus dimensionless advection erosion number (N_{ae}—equation (12)) for all of the models supports the observation that slip rate and erosion efficiency both play a role in the development of characteristic landscape morphologies in strike-slip settings. Figure 5 shows an inverse correlation between PRR and N_{ae}, with a maximum PRR value of ~1 for N_{ae} values of ~1 or less. Results from the suite of model experiments with a nonlinear hillslope transport function (black symbols Figure 5) show that PRR values from these simulations plot in similar positions to the equivalent linear models and suggest that thresholds in slope do not significantly alter the overall geomorphic patterns that develop in response to strike-slip faulting. In addition, simulations with a larger model domain (12,000 m × 600 m with 5 m resolution), slower uplift rates (0.5 mm/yr), and original grid size but with a higher resolution (4000 m × 200 m with 3 m resolution) also show no obvious deviations in behavior from the main suite of models (Figure 5).

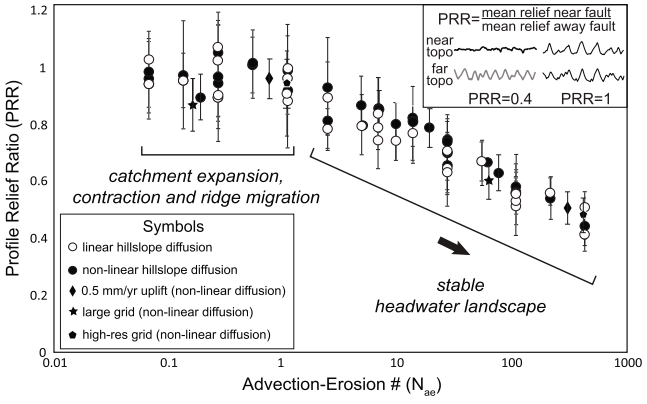

Figure 5. Plot of mean profile relief ratio versus advection-erosion number for all strike-slip model runs. PRR is calculated at each output step for all model runs. Uncertainty on mean PRR (vertical error bars) represents variability in PRR at each time step. Upper inset shows how PRR is calculated using example near- fault and far-fault topographic profiles (see Figure 3).

We also plot PRR values against the advection-uplift number (N_{au}—equation (11)) for all model runs to consider the importance of the ratio of horizontal to vertical fault motion

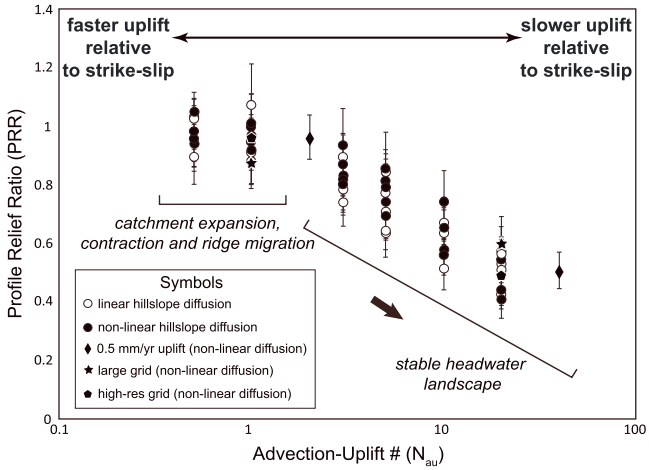

Figure 6. Plot of mean profile relief ratio versus advection-uplift number for all strike-slip model runs. Low N_{au} numbers (left side of plot) reflect faster uplift to horizontal advection ratios, and high N_{au} numbers (right side of plot) reflect slower uplift to horizontal advection ratios. PRR is calculated at each output step for all model runs. Uncertainty on mean PRR (vertical error bars) represents variability in PRR at each time step.

on strike-slip landscape evolution. Results show a trend similar to the plot of PRR and N_{ae} (Figure 5): PRR inversely correlates with N_{au}, with maximum PRR values of ~1 for N_{au} at or <1 and consistency among linear hillslope models, experiments with larger domain sizes, and higher-resolution grids (Figure 6). The simulations with a 0.5 mm/yr regional uplift rate (black diamonds) plot to the left of the models run with the same horizontal slip rate but 1 mm/yr uplift rate, which supports the assertion that increasing the ratio of advection to uplift (N_{au}) acts to reduce ridge mobility.

4. Discussion

Studying the patterns and form of hillslopes and rivers that drain uplifting mountain ranges provides an established means to assess vertical tectonic movements of crust [e.g., *Hack*, 1973; *Seeber and Gornitz*, 1983; *Merritts and Vincent*, 1989; *Whipple and Tucker*, 1999; *Wobus et al*., 2006; *Kirby and Whipple*, 2012]. Our work indicates that the landscape also encodes information related specifically to horizontal crustal motion along strike-slip faults. Surface morphologies both proximal to and upstream of strike-slip faults evolve in response to the cycle of river lengthening and shortening associated with lateral fault offset. The distinct landscapes shown in Figures 2 and 3 reflect this competition between horizontal advection (strike-slip fault rate) and the transient landscape response to the new baselevel conditions (represented by N_{ae}—equation (12)).

When slip rate is slow and/or hillslope diffusion and channel incision are efficient (N_{ae} ~1) the pace of landscape adjustment to strike-slip faulting is rapid enough to allow the growth of new catchments in response to river lengthening and horizontal advection of topography. As a consequence, drainage density and ridge spacing at these settings vary in time and space. When slip rate is fast and/or hillslope diffusion and channel incision are inefficient, advection outpaces erosion ($N_{ae} \gg 1$). In these cases, the headwater reaches are stable and ridge spacing is more regular because the response time of the fault-adjacent landscape to lengthening along the main channel is too long to allow new catchment growth upstream of the fault before the next river capture occurs, "resetting" the landscape and starting the cycle anew.

The relative rate of uplift or baselevel fall also appears to affect ridge mobility. Simulations with faster uplift relative to strike-slip (lower N_{au}) have higher PRR values, and thus greater ridge mobility, than simulations with slower uplift relative to strike slip (Figure 6). This observation seems to run counter to intuition, for if horizontal fault motion ultimately drives ridge mobility then one would expect a lower rate of strike-slip to uplift to dampen, not enhance, this effect. However, as evident from the advection term in the generic form of the governing equation (equation (5)), horizontal bedrock motion has a greater effect when topographic gradients parallel to the direction of tectonic transport are large. Because vertical rather than horizontal motion generates this relief, regional uplift, even if it predates strike-slip faulting, is an important component to the catchment response to strike-slip faulting.

Previous studies have shown that ridge migration occurs in response to local differences in erosion rates, often due to a contrast in relief on opposing sides of a divide [e.g., *Gilbert*, 1880; *Tucker and Slingerland*, 1994; *Harbor*, 1997; *Hasbargen and Paola*, 2000; *Mudd and Furbish*, 2005; *Willett et al*., 2014] and that transient ridge migration is expected among neighboring basins that are competing for drainage area as they adjust to an equilibrium landscape with uniform valley spacing [*Perron et al*., 2008, 2009]. Our analysis predicts that given topography and enough time for changing base-level conditions to propagate, strike-slip fault landscapes should show a similar adjustment that includes ridge-migration and catchment

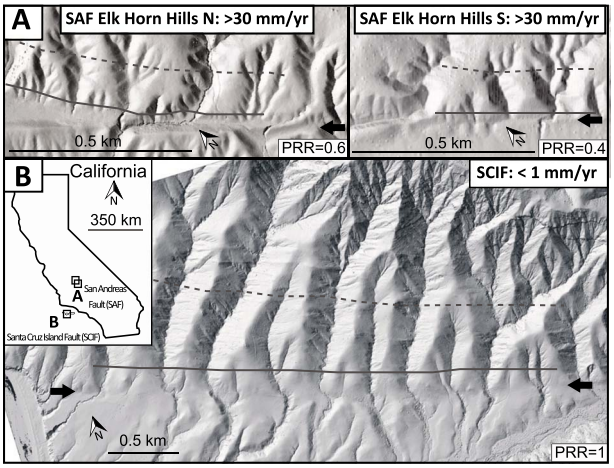

Figure 7. Bare Earth lidar of (a) the South and North Elk Horn Hills sections of the dextral San Andreas Fault (SAF) and (b) the sinistral Santa Cruz Island Fault. Black arrows indicate fault location. Solid and dashed lines depict location of topographic profiles used in the PRR calculation (see text for details). Inset map shows field site locations in California.

expansion. Local disequilibrium in erosion arises in strike-slip settings from both the expansion and contraction of catchments and the lengthening and shortening of the trunk channels. An important distinction among landscape types, however, is that the disequilibrium associated with strike-slip settings should persist for as long as the fault is active. In contrast, landscapes that are adjusting to baselevel change associated with mountain uplift should eventually reach a steady form, albeit more slowly depending on the horizontal component in the velocity field [*Willett et al*., 2001].

Offset rivers are commonly relied upon to indicate fault locations and to calculate slip rates. However, stream capture events are known to limit the maximum offset recorded by rivers flowing along a fault and as a result can erase or skew our interpretation of sense of fault slip, offset magnitude, and slip rate [*Huang*, 1993; *Lacassin et al*., 1998; *Walker and Allen*, 2012]. The distinctive surface forms associated with strike-slip faulting revealed by our models result from the transient response to these capture events as well as to the phase of river lengthening in the strike-slip cycle. Thus, they should serve as additional and potentially more robust indicators of fault activity because they will be preserved in the landscape for longer periods of time.

Comparison of well-known faults in California that slip at different rates reveals similarities with the model landscapes. The San Andreas Fault is a right-lateral continental transform boundary that separates the Pacific and North American plates for a length of ~1300 km at a rate greater than 30 mm/yr [*Sieh and Jahns*, 1984]. In contrast, the Santa Cruz Island Fault is a left-lateral fault that extends for ~ 35 km and slips at a much lower rate of ~1 mm/yr or less [*Pinter et al*., 1998]. At both field sites, obvious laterally deflected stream channels demarcate the faults, but differences in fault valleys and fault-adjacent hillslope character are also observable (Figure 7). Steep fault-facing slopes and a well-developed fault valley with sharply offset ridges occurs along the Elk Horn Hills segments of the San Andreas Fault in northern CA (Figure 7a). In contrast, faceted spurs are less prominent along the slower-slipping Santa Cruz Island Fault, where ridges can be traced across the fault (Figure 5b). Catchments near to and upstream of this fault also show variability in size, orientation, and spacing, similar to what we expect if drainage reorganization and ridge migration is occurring in response to strike-slip faulting.

For a more quantitative comparison, we also calculated profile relief ratios for each of the study sites. PRR was determined by finding the minimum and maximum elevations from lidar digital elevation model data along topographic profiles near to and farther from the faults. We applied the same scaling as in the modeled landscapes in order to position each profile: near-fault profiles were located at a distance from the fault equivalent to 10% of the total distance from fault to main drainage divide and far-fault profiles were located at a distance from the fault equivalent to 50% of the total distance from fault to main drainage divide (Figure 7). Calculated profile relief ratios of 0.6 and 0.4 for the fast-slipping Elk Horn Hills segments of the San Andreas Fault and a PRR of 1 for the slower-slipping Santa Cruz Island Fault match well with model predictions.

As predicted by our model results, differences in horizontal slip rate offer a reasonable explanation for the observed landscape patterns and PRR values among the compared CA faults. These findings highlight the potential to extract slip-rate information directly from surface morphologies. However, we expect that variability in fault age, total offset, dip-slip deformation, rock erodibility/diffusivity, or climate, none of which were accounted for at these field locations, may also influence the geomorphology of strike-slip fault zones. Accordingly, further in-depth field studies at sites with a range of known tectonic, lithologic, and climatic variables are needed to more fully understand how strike-slip tectonics is imprinted in the landscape.

5. Conclusions

Landscape evolution modeling to investigate the longer-term, catchment-wide landscape response to horizontal fault motion demonstrates that strike-slip faulting induces a state of landscape disequilibrium that continues for as long as the fault is active. Comparison of a suite of models with different horizontal slip rates, bedrock erodibility, hillslope diffusivity, and regional uplift rate shows a range of landscape patterns and geomorphic response to lateral forcing. These promising results suggest that in addition to the long-observed process of river offset along active strike-slip faults, analysis of near-fault landforms, such as ridges and facets, as well as the catchments upstream of strike-slip faults, has the potential to reveal important information about tectonic rates and surface processes.

Results from this study also suggest that the long-term geomorphic response to strike-slip faulting could be an important yet underappreciated component of landscape development at the orogenic scale. Many of the world's active mountain belts are deformed by large strike-slip faults (e.g., Tibet, west coast of N. America, and New Zealand) but only a limited number of studies of landscape evolution [e.g., *Anderson*, 1990; *Braun and Sambridge*, 1997; *Willett et al*., 2001; *Miller and Slingerland*, 2006; *Castelltort et al*., 2012] consider any horizontal component of deformation in addition to the vertical. Our findings underscore the need to further consider the role of tectonic advection in long-term landscape evolution, especially in strike-slip settings where motion is dominantly horizontal.

Acknowledgments

The data for this paper are available by contacting the corresponding author at aduvall@uw.edu. We acknowledge the National Geographic Society and the National Science Foundation (grant EAR–1321859) for support of this research. A.D. received funding through a CIRES fellowship. We thank Alex Lechler for assistance with MATLAB code and Ramon Arrowsmith and Camille Collett for suggesting possible field localities for model comparison. Thorough and insightful comments from Scott Miller, Mikael Attal, an anonymous reviewer and Associate Editor Noah Finnegan greatly improved the manuscript.

References

Anderson, R. S. (1990), Evolution of the northern Santa Cruz Mountains by advection of crust past a San Andreas Fault bend, *Science*, *249*, 397–401.

Andrews, D. J., and R. C. Bucknam (1987), Fitting degradation of shorelines scarps by a nonlinear diffusion model, *J. Geophys. Res.*, *110*(B12), 12,857–12,867, doi:10.1029/JB092iB12p12857.

Berryman, K. (1990), Late Quaternary movement on the Wellington Fault in the Upper Hutt area, New Zealand, *N.Z. J. Geol. Geophys.*, *33*, 257–270.

Braun, J., and M. Sambridge (1997), Modelling landscape evolution on geological time scales: A new method based on irregular spatial discretization, *Basin Res.*, *9*(1), 27–52.

Castelltort, S., L. Goren, S. D. Willett, J. D. Champagnac, F. Herman, and J. Braun (2012), River drainage patterns in the NZ Alps primarily controlled by plate tectonic strain, *Nat. Geosci.*, *5*, 744–748.

Cowgill, E. (2007), Impact of riser reconstructions on estimation of secular variation in rates of strike-slip faulting: Revisiting the Cherchen River site along the Altyn Tagh Fault, NW China, *Earth Planet. Sci. Lett.*, *254*, 239–255.

Culling, W. E. H. (1960), Analytical theory of erosion, *J. Geol.*, *68*(3), 336–344.

Dorsey, R. J., and J. J. Roering (2006), Quaternary landscape evolution in the San Jacinto fault zone, Peninsular Ranges of Southern California: Transient response to strike-slip initiation, *Geomorphology*, *73*(1–2), 16–32.

Gaudemer, Y., P. Tapponnier, and D. L. Turcotte (1989), River offsets across active strike-slip faults, *Ann. Tecton.*, *3*(2A), 55–76.

Gilbert, G. K. (1880), *Report on the Geology of the Henry Mountains*, 170 pp., Govt. Print. Off., Washington D. C.

Gold, R. D., E. Cowgill, J. R. Arrowsmith, J. Gosse, X. Chen, and X.-F. Wang (2009), Riser diachroneity, lateral erosion, and uncertainty in rates of strike-slip faulting: A case study from Tuzidun along the Altyn Tagh Fault, NW China, *J. Geophys. Res.*, *114*, B04401, doi:10.1029/2008JB005913.

Goren, L., S. D. Willett, F. Herman, and J. Braun (2014), Coupled numerical-analytical approach to landscape evolution modeling, *Earth Surf. Processes Landforms*, *39*(4), 522–545.

Hack, J. T. (1973), Stream-profile analysis and stream-gradient index, *J. Res. U.S. Geol. Surv.*, *1*(4), 421–429.

Harbor, D. J. (1997), Landscape evolution at the margin of the Basin and Range, *Geology*, *25*, 1111–1114.

Hasbargen, L. E., and C. Paola (2000), Landscape instability in an experimental drainage basin, *Geology*, *28*, 1067–1070.

Hill, M. L., and T. W. Dibblee (1953), San Andreas, Garlock, and Bing Pine Faults, California—A study of character, history, and tectonic significance of their displacements, *Geol. Soc. Am. Bull.*, *64*, 443–458.

Howard, A. D. (1994), A detachment-limited model of drainage basin evolution, *Water Resour. Res.*, *30*, 2261–2285, doi:10.1029/94WR00757.

Huang, W. (1993), Morphologic patterns of stream channels on the active Yishi Fault, southern Shandong Province, Eastern China: Implications for repeated great earthquakes in the Holocene, *Tectonophysics*, *219*, 283–304.

Hubert-Ferrari, A., Armijo, R., King, G., Meyer, B., and Barka, A. (2002), Morphology, displacement, and slip rates along the North Anatolian Fault, Turkey, *J. Geophys. Res.*, *107*(B10), 2235, doi:10.1029/2001JB000393.

Kirby, E., and K. X. Whipple (2012), Expression of active tectonics in erosional landscapes, *J. Struct. Geol.*, *44*, 54–75.

Kooi, H., and C. Beaumont (1994), Escarpment evolution on high-elevation rifted margins: Insights derived from a surface processes model that combines diffusion, advection, and reaction, *J. Geophys. Res.*, *99*, 12,191–12,209, doi:10.1029/94JB00047.

Koons, P. O. (1994), Three-dimensional critical wedges: Tectonics and topography in oblique collisional orogens, *J. Geophys. Res.*, *99*, 12,301–12,315, doi:10.1029/94JB00611.

Lacassin, R., A. Replumaz, and P. H. Leloup (1998), Hairpin river loops and slip-sense inversion on southeast Asian strike-slip faults, *Geology*, *26*, 703–706.

Mann, P., C. S. Prentice, G. Burr, L. R. Peña, and F. W. Taylor (1998), Tectonic geomorphology and paleoseismology of the Septentrional fault system, Dominican Republic, in *Active Strike-Slip and Collisional Tectonics of the Northern Caribbean Plate Boundary Zone*, edited by J. F. Dolan and P. Mann, *Geol. Soc. Am. Spec. Pap.*, 326, 63–123.

Mériaux, A.-S., F. J. Ryerson, P. Tapponnier, J. Van der Woerd, R. C. Finkel, X. Xu, Z. Xu, and M. W. Caffee (2004), Rapid slip along the central Altyn Tagh Fault: Morphochronologic evidence from Cherchen He and Sulamu Tagh, *J. Geophys. Res.*, *109*, B06401, doi:10.1029/2003JB002558.

Merritts, D., and K. R. Vincent (1989), Geomorphic response of coastal streams to low, intermediate, and high rates of uplift, Mendocino trip junction region, northern California, *Geol. Soc. Am. Bull.*, *101*(11), 1373–1388.

Miller, S. R., and R. L. Slingerland (2006), Topographic advection on fault-bend folds: Inheritance of valley positions and the formation of wind gaps, *Geology*, *34*, 769–772.
Mudd, S. M., and D. J. Furbish (2005), Lateral migration of hillcrests in response to channel incision in soil-mantled landscapes, *J. Geophys. Res.*, *110*, F04026, doi:10.1029/2005JF000313.
Ouchi, S. (2004), Flume experiments on the horizontal stream offset by strike-slip faults, *Earth Surf. Processes Landforms*, *29*, 161–173.
Ouchi, S. (2005), Development of offset channels across the San Andreas fault, *Geomorphology*, *70*, 112–128.
Perron, J. T., W. E. Dietrich, and J. W. Kirchner (2008), Controls on the spacing of first-order valleys, *J. Geophys. Res.*, *113*, F04016, doi:10.1029/2007JF000977.
Perron, J. T., W. E. Dietrich, and J. W. Kirchner (2009), Formation of evenly spaced ridges and valleys, *Nature*, *460*, doi:10.1038/nature08174.
Pinter, N., S. B. Lueddecke, E. A. Keller, and K. R. Simmons (1998), Late quaternary slip on the Santa Cruz Island fault, California, *Geol. Soc. Am. Bull.*, *110*, 711–722.
Press, W. H., B. P. Flannery, S. A. Teukolsky, and W. T. Vetterling (1992), *Numerical Recipes in Fortran: The Art of Scientific Computing*, 2nd ed., pp. 444–455, Cambrige Univ. Press, New York.
Replumaz, A., R. Lacassin, P. Tapponnier, and P. H. Leloup (2001), Large river offsets and Plio-Quaternary dextral slip rate on the Red River fault (Yunnan, China), *J. Geophys. Res.*, *106*(B1), 819–836, doi:10.1029/2000JB900135.
Roering, J. J., J. W. Kirchner, and W. E. Dietrich (1999), Evidence for nonlinear, diffusive sediment transport on hillslopes and implications for landscape morphology, *Water Resour. Res.*, *35*, 853–870, doi:10.1029/1998WR900090.
Roy, S. G., P. O. Koons, P. Upton, and G. E. Tucker (2015), The influence of crustal strength fields on the patterns and rates of fluvial incision, *J. Geophys. Res. Earth Surf.*, *120*, 275–299, doi:10.1002/2014JF003281.
Seeber, L., and V. Gornitz (1983), River profiles along the Himalayan arc as indicators of active tectonics, *Tectonophysics*, *92*(4), 335–367.
Seidl, M. A., and W. E. Dietrich (1992), The problem of bedrock channel erosion, *Catena Suppl.*, *23*, 101–124.
Sieh, K. E., and R. H. Jahns (1984), Holocene activity of the San Andreas fault at Wallace creek, California, *Geol. Soc. Am. Bull.*, *95*, 883–896.
Tucker, G. E. (2004), Drainage basin sensitivity to tectonic and climatic forcing: Implications of a stochastic model for the role of entrainment and erosion thresholds, *Earth Surf. Processes Landforms*, *29*(2), 185–205.
Tucker, G. E., and R. L. Bras (2000), A stochastic approach to modeling the role of rainfall variability in drainage basin evolution, *Water Resour. Res.*, *36*(7), 1953–1964, doi:10.1029/2000WR900065.
Tucker, G. E., and R. L. Slingerland (1994), Erosional dynamics, flexural isostasy, and long-lived escarpments: A numerical modeling study, *J. Geophys. Res.*, *99*, 12,229–12,243, doi:10.1029/94JB00320.
Tucker, G. E., S. T. Lancaster, N. M. Gasparini, R. L. Bras, and S. M. Rybarczyk (2001a), An object oriented framework for hydrologic and geomorphic modeling using triangulated irregular networks, *Comput. Geosci.*, *27*(8), 959–973.
Tucker, G., S. Lancaster, N. Gasparini, and R. Bras (2001b), The channel-hillslopes integrated landscape development model (CHILD), in *Landscape Erosion and Evolution Modeling*, edited by R. S. Harmon and W. W. Doe III, pp. 349–388, Kluwer Acad./Plenum, New York.
Van Der Woerd, J., P. Tapponnier, F. J. Ryerson, A.-S. Meriaux, B. Meyer, Y. Gaudemer, R. C. Finkel, M. W. Caffee, G. Zhao, and Z. Xu (2002), Uniform postglacial slip-rate along the central 600 km of the Kunlun fault (Tibet), from 26Al, 10Be and 14C dating of riser offsets, and climatic origin of the regional morphology, *Geophys. J. Int.*, *148*, 356–388.
Walker, F., and M. B. Allen (2012), Offset rivers, drainage spacing and the record of strike-slip faulting: The Kuh Banan Fault, Iran, *Tectonophysics*, *530*, 251–263.
Wallace, R. E. (1949), Structure of a portion of the San Andreas rift in southern California, *Geol. Soc. Am. Bull.*, *60*, 781–806.
Wallace, R. E. (1968), Notes on stream channel offset by the San Andreas fault, southern Coast Ranges, California, in *Conference on Geologic Problems of the San Andreas Fault System*, vol. 11, pp. 6–21, Stanford Univ. Publication in Geological Sciences, Stanford.
Weldon, R. J., and K. E. Sieh (1985), Holocene rate of slip and tentative recurrence interval for large earthquakes on the San Andreas fault, Cajon Pass, southern California, *Geol. Soc. Am. Bull.*, *96*, 793–812.
Whipple, K. X., and G. E. Tucker (1999), Dynamics of the stream-power river incision model: Implications for height limits of mountain ranges, landscape response timescales, and research "needs", *J. Geophys. Res.*, *104*(B8), 17,661–17,674, doi:10.1029/1999JB900120.
Willett, S. D., R. Slingerland, and N. Hovius (2001), Uplift, shortening, and steady state topography in active mountain belts, *Am. J. Sci.*, *301*(4–5), 455–485.
Willett, S. D., S. W. McCoy, J. T. Perron, L. Goren, and C. Y. Chen (2014), Dynamic reorganization of river basins, *Science*, *343*, doi:10.1126/science.1248765.
Wobus, C., K. X. Whipple, E. Kirby, N. Snyder, J. Johnson, K. Spyropolou, and D. Sheehan (2006), Tectonics from topography: Procedures, promise, and pitfalls, *Geol. Soc. Am. Spec. Pap.*, *398*, 55–74.
Zielke, O., J. R. Arrowsmith, L. G. Ludwig, and S. O. Akciz (2010), Slip in the 1857 and Earlier Large Earthquakes Along the Carrizo Plain, San Andreas Fault, *Science*, *327*(5969), 1119–1122.